

General analytical algorithm of mechanical properties for $1H$ - MX_2 transition metal dioxides and dichalcogenides

Dong Li^{1,2}, Junfei Zhao,¹ Yonggang Zheng,¹ Hongwu Zhang,¹ and Hongfei Ye^{1,*}

¹International Research Center for Computational Mechanics, State Key Laboratory of Structural Analysis, Optimization and CAE Software for Industrial Equipment, Department of Engineering Mechanics, Faculty of Vehicle Engineering and Mechanics, Dalian University of Technology, Dalian 116024, People's Republic of China

²State Key Laboratory Mine Response and Disaster Prevention and Control in Deep Coal Mine, Anhui University of Science and Technology, Huainan 232001, People's Republic of China



(Received 13 July 2023; revised 20 September 2023; accepted 22 September 2023; published 11 October 2023)

2D transition-metal dioxides and dichalcogenides with $1H$ phase ($1H$ - MX_2) have a large number of members and a wide range of material properties, making them promising candidates for numerous applications. The comprehensive, accurate, and rapid evaluation on the mechanical properties of the $1H$ - MX_2 family has been an important and challenging issue. Here, a general theoretical model is constructed based on molecular mechanics, which provides an accurate and rapid analytical algorithm for calculating the mechanical properties of the entire family of $1H$ - MX_2 . The validity of the constructed model is verified by molecular dynamics simulations upon the scale effect on the mechanical behavior of $1H$ - MoS_2 . Notably, we report a library composed of the mechanical properties of 34 types of $1H$ - MX_2 . It is found that the mechanical performances of $1H$ - MX_2 depend on the period and group numbers of elements. The obtained results are in good agreement with the existing experimental and numerical results. Furthermore, the roles of molecular structure and force field on the mechanical properties are elucidated, which is beneficial in predicting the mechanical performances of the potential and unreported $1H$ - MX_2 . The findings offer an important theoretical basis for the reverse design and optimization of $1H$ - MX_2 material-based nanodevices through nanostructure-property relationships.

DOI: [10.1103/PhysRevB.108.144103](https://doi.org/10.1103/PhysRevB.108.144103)

I. INTRODUCTION

In recent years, two-dimensional (2D) materials have sparked great interest from the perspective of basic physics and applied science [1–4]. Graphene, a typical 2D material, is quite popular because of its many fascinating properties, but the lack of electronic band gap stimulates the search for other 2D materials with semiconducting performances [5–7]. The latest studies have revealed that 2D transition-metal dioxides and dichalcogenides with the generalized formula MX_2 (M is a transition metal atom, and X is a chalcogen atom) might offer properties superior to graphene [2,8,9]. More than 60 transition metal dichalcogenides have been discovered, and at least 40 of them have layered crystal structures [8,10]. It is notable that MX_2 exists in several structural phases according to different coordination spheres of the transition metal atoms. Some of the monolayer MX_2 have D_{3h} point group symmetry and are specified as $1H$ phase [11,12]. Compared to the $1T$ phase with D_{3d} point group symmetry, the $1H$ phase has higher stability and wider application [13,14]. Among the $1H$ - MX_2 materials, $1H$ - MoS_2 is the most presentative material due to its robustness and the high availability of raw materials [14,15].

The $1H$ - MX_2 compounds often exhibit many excellent properties and hold promise for a broad range of appli-

cations in integrated circuits and nanoelectronics [2,16,17]. Interestingly, mechanical strain can strongly perturb the band structure of these materials, which opens up a new avenue to further improve material properties and prepare on-demand devices [18,19]. Therefore, a full understanding of the mechanical properties and deformation behaviors of $1H$ - MX_2 is essential to design and adjust their mechanical and electrical performances reasonably. The probe microscopy technique provides an effective way to operate and measure 2D materials at the nanoscale [20–22]. Cooper *et al.* measured the surface elastic modulus and intrinsic strength of $1H$ - MoS_2 based on the nanoindentation experiments, and the results are close to Griffith's prediction on strength limit [21]. Yang *et al.* conducted tensile tests on $1H$ - $MoSe_2$ based on the developed *in situ* nanomechanical platform and observed the brittle fracture processes of crack initiation, propagation, and final failure in real time [22]. Although considerable progress has been made in the control accuracy of equipment, it is still a formidable task to directly determine the mechanical properties of 2D materials at the nanoscale based on experimental methods, especially for so many family members [23,24].

With the improvement of computer performance, numerical calculations play an increasingly important role in exploring the mechanical property and its underlying mechanism of 2D materials, such as first-principles calculations, molecular mechanics (MM), and molecular dynamics (MD) simulations [25–28]. Çakır *et al.* predicted the mechanical and thermal properties of $1H$ - MX_2 ($M = \text{Cr, Mo, W}$; $X =$

*Corresponding author: yehf@dlut.edu.cn

O, S, Se, Te) based on the density functional theory, and the obtained results are quite consistent with the experiments [25]. Kang *et al.* examined the in-plane mechanical properties of $1H-MX_2$ by utilizing the first-principles calculation. The research indicates that the in-plane stiffness decreases when X changes from S to Te and M changes from W to Mo [29]. Jiang *et al.* evaluated the mechanical properties of $1H-MoS_2$, including the elastic modulus, Poisson's ratio, and bending stiffness, using an analytic formula on the basis of the MM method [30,31]. Li *et al.* investigated the bending behaviors of $1H-MoS_2$ based on MD simulations and revealed the size-dependent bending stiffness caused by the boundary effect [32]. The above researches provide valuable insights into the mechanical behavior of several representative $1H-MX_2$ materials. However, $1H-MX_2$ covers a large family of materials, and there are still many members whose mechanical properties have not yet been reported. Furthermore, there are also considerable costs associated with developing and designing specific experiments and algorithms for individual materials. Therefore, it is of great significance to construct a general model for the comprehensive and rapid evaluation on mechanical properties of the $1H-MX_2$ family based on their molecular structures.

In this work, based on the MM framework, a general analytical algorithm (theoretical model) is proposed for evaluating the mechanical properties of $1H-MX_2$, including surface elastic and shear moduli and in-plane and out-of-plane Poisson's ratios. On the basis of the study of mechanical behaviors of $1H-MoS_2$, the constructed model is verified by MD simulations. Moreover, we predict the mechanical properties of 34 types of $1H-MX_2$, and the obtained results are in good agreement with the existing experimental, DFT, and MD methods. Furthermore, the effects of geometrical structure and force-constant parameters on mechanical performances are examined here. This work offers an effective and rapid computational method to assess the mechanical properties of $1H-MX_2$ materials.

II. MODELS AND METHODOLOGY

A. Theoretical basis

The general theoretical model is established based on a MM framework. In the MM method, the molecule is regarded as a group of atoms held together by interatomic interaction, and the intermolecular interactions are calculated through the van der Waals and electrostatic potentials [33,34]. Hence, the total system potential can be expressed as a sum of several individual energy terms,

$$E_{\text{total}} = E_{\text{bond}} + E_{\text{angle}} + E_{\text{inv}} + E_{\text{tor}} + E_{\text{vdW}} + E_{\text{ele}}, \quad (1)$$

where E_{bond} , E_{angle} , E_{inv} , and E_{tor} are the energies associated with bond stretching, bond angle bending, inversion, and torsion, respectively. E_{vdW} and E_{ele} are associated with van der Waals and electrostatic interactions, respectively. It should be noted that bond stretching and bond angle bending are typical motion styles for most covalent bonding materials, which play dominant roles in the total system potential. Thus, the total system potential can be reduced to the sum of the two energy terms (E_{bond} and E_{angle}) [30,33,35].

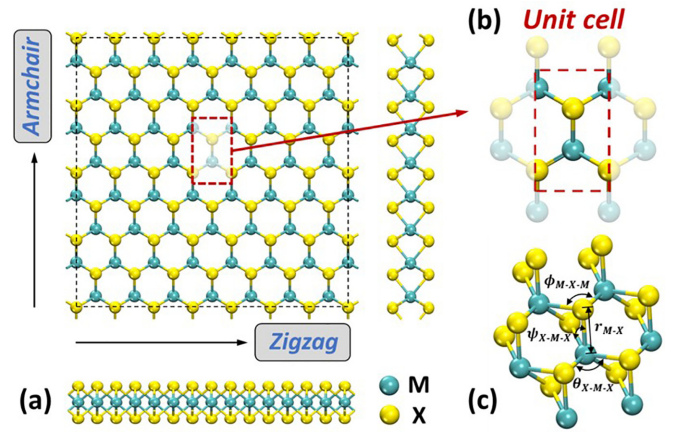


FIG. 1. The molecular configuration of $1H-MX_2$. (a) The structure of $1H-MX_2$ with different chiral directions. (b) The selected unit cell is in the red rectangle. (c) The perspective view of the unit cell with geometrical variables.

According to the Born-Oppenheimer approximation, the system potential can be expressed as a function of atomic coordinates. Figure 1(a) shows the molecular configuration of $1H-MX_2$ with D_{3h} point group symmetry, which consists of three atomic layers with a transition metal atom sandwiched between two chalcogen atoms. Based on the boundary characteristics of $1H-MX_2$, the chiral directions can be divided into the armchair and zigzag types. For the convenience of calculation, we select a representative unit cell labeled by the red rectangle in Fig. 1(b), and the corresponding geometrical variables are shown in Fig. 1(c). There are one type of bond length and three types of bond angles in the unit cell, which are defined as $M-X$ bond length (r), $M-X-M$ intralayer angle (ϕ), $X-M-X$ intralayer angle (θ), and $X-M-X$ interlayer angle (ψ), respectively. In this work, we examine the elastic properties of $1H-MX_2$ materials under the small deformation conditions and find that the harmonic function is sufficient to characterize the related mechanical properties [30,33,34]. Thus, the total potential energy (E) of $1H-MX_2$ can be further expressed as follows:

$$E_{\text{total}} = \frac{1}{2} \sum K_r dr^2 + \frac{1}{2} \sum K_\phi d\phi^2 + \frac{1}{2} \sum K_\theta d\theta^2 + \frac{1}{2} \sum K_\psi d\psi^2, \quad (2)$$

where K_r , K_ϕ , K_θ , and K_ψ are the force-constant parameters of bond length and bond angles.

It is worth noting that the potential energy of the unit cell at the inner and boundary is different due to the dangling bonds [32,36]. Hence, for $1H-MX_2$ with the nonperiodic boundary, the potential energy is calculated by considering the effective bond lengths and bond angles without taking into account the dangling bonds, which means that the proposed computational model can describe the size-dependent mechanical properties. Under the external loading (W), the total energy (U) can be given as

$$U = E_{\text{inner}} + E_{\text{bound}} - W, \quad (3)$$

where E_{inner} and E_{bound} are the potential energies of the unit cell at the inner and boundary. It should be noted that due

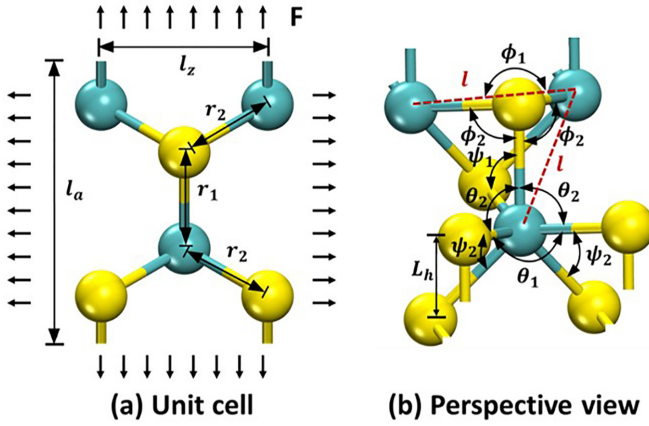


FIG. 2. The distribution of different types of bond lengths and bond angles of unit cell under the tension deformation. The black arrows represent the directions of the loadings. The red dashed lines are auxiliary lines.

to the controversial thickness of 2D materials, the surface modulus (unit: N/m) is calculated here to characterize the mechanical performance of the relevant materials. Based on the principle of minimum potential energy ($\delta U = 0$), the analytical algorithms are constructed for evaluating the surface elastic and shear moduli, in-plane and out-of-plane Poisson's ratios under the uniaxial tension, and pure shear conditions, respectively.

B. Tension model

The uniaxial tension loading is applied along different chiral directions of the unit cell, as shown in Fig. 2(a). Based on the structural symmetry of $1H-MX_2$, the tension deformation of the unit cell can be characterized by two groups of variables (r_i , ϕ_i , θ_i , and ψ_i , where $\phi_i = \theta_i$, $i = 1, 2$), as depicted in Fig. 2(b). During the tensile process, the structural relationship of $1H-MX_2$ satisfies the small deformation assumption. Subsequently, we will derive the geometrical relationships between these variables to construct expressions for the total energy. According to the consistency of thickness, the variables (r_i and ψ_i) should satisfy

$$r_1 \sin \frac{\psi_1}{2} = r_2 \sin \frac{\psi_2}{2}. \quad (4)$$

Differentiating both sides of Eq. (4) leads to

$$dr_2 = A_1 d\psi_1 + A_2 d\psi_2 + A_3 dr_1, \quad (5)$$

where

$$A_1 = \frac{r_1 \cos \frac{\psi_1}{2}}{2 \sin \frac{\psi_2}{2}}, \quad A_2 = -\frac{r_2 \cot \frac{\psi_2}{2}}{2}, \quad A_3 = \frac{\sin \frac{\psi_1}{2}}{\sin \frac{\psi_2}{2}}. \quad (6)$$

Based on the geometrical relationships, the distance l between adjacent M atoms in the unit cell can be expressed as

$$\begin{aligned} l^2 &= r_1^2 + r_2^2 - 2r_1 r_2 \cos \phi_2 \\ &= \left[r_1 \cos \frac{\psi_1}{2} + \sqrt{\left(r_2 \cos \frac{\psi_2}{2} \right)^2 - \left(r_2 \sin \frac{\phi_1}{2} \right)^2} \right]^2 \\ &\quad + \left(r_2 \sin \frac{\phi_1}{2} \right)^2. \end{aligned} \quad (7)$$

Equation (4) is substituted into Eq. (7), and then differentiating Eq. (7) leads to

$$d\psi_2 = B_1 d\phi_1 + B_2 d\phi_2 + B_3 d\psi_1, \quad (8)$$

where

$$\begin{aligned} B_1 &= -\frac{(1 + \cos \psi_1) \sin \phi_1}{2(\sin \psi_2 - 2 \cos \phi_2 \sin \frac{\psi_1}{2} \cos \frac{\psi_2}{2})}, \\ B_2 &= -\frac{4 \sin \phi_2 (\sin \frac{\psi_1}{2} \sin \frac{\psi_2}{2} - \cos \phi_2)}{\sin \psi_2 - 2 \cos \phi_2 \sin \frac{\psi_1}{2} \cos \frac{\psi_2}{2}}, \\ B_3 &= -\frac{\sin \psi_1 (1 + \cos \phi_1) - 4 \cos \phi_2 \cos \frac{\psi_1}{2} \sin \frac{\psi_2}{2}}{2(\sin \psi_2 - 2 \cos \phi_2 \sin \frac{\psi_1}{2} \cos \frac{\psi_2}{2})}. \end{aligned} \quad (9)$$

Substituting Eq. (8) into Eq. (5),

$$dr_2 = C_1 d\phi_1 + C_2 d\phi_2 + C_3 d\psi_1 + C_4 dr_1, \quad (10)$$

where

$$C_1 = A_2 B_1, C_2 = A_2 B_2, C_3 = A_1 + A_2 B_3, C_4 = A_3. \quad (11)$$

In the unit cell, l_a and l_z are the sizes along the armchair and zigzag directions, respectively. L_h is the thickness of monolayer $1H-MX_2$. For $1H-MX_2[m, n]$ with a finite size (m and n are the amounts of unit cell in two chiral directions), the sizes of the whole $1H-MX_2$ can be written as

$$\begin{aligned} L_a &= m \left(2r_1 \cos \frac{\psi_1}{2} + \sqrt{2} r_2 \sqrt{\cos \psi_2 + \cos \phi_1} \right) - r_1 \cos \frac{\psi_1}{2}, \\ L_z &= 2nr_2 \sin \frac{\phi_1}{2}, \\ L_h &= 2r_1 \sin \frac{\psi_1}{2}. \end{aligned} \quad (12)$$

Differentiating Eq. (12), and combining Eqs. (8) and (10) leads to

$$\begin{aligned} dL_a &= D_1 d\phi_1 + D_2 d\phi_2 + D_3 d\psi_1 + D_4 dr_1, \\ dL_z &= D_5 d\phi_1 + D_6 d\phi_2 + D_7 d\psi_1 + D_8 dr_1, \\ dL_h &= D_9 d\phi_1 + D_{10} d\phi_2 + D_{11} d\psi_1 + D_{12} dr_1, \end{aligned} \quad (13)$$

where

$$\begin{aligned} D_1 &= m \left[C_1 \sqrt{2(\cos \psi_2 + \cos \phi_1)} - \frac{r_2 (\sin \phi_1 + B_1 \sin \psi_2)}{\sqrt{2(\cos \psi_2 + \cos \phi_1)}} \right], \\ D_2 &= m \left[C_2 \sqrt{2(\cos \psi_2 + \cos \phi_1)} - \frac{B_2 r_2 \sin \psi_2}{\sqrt{2(\cos \psi_2 + \cos \phi_1)}} \right], \end{aligned}$$

$$\begin{aligned}
D_3 &= m \left[-r_1 \sin \frac{\psi_1}{2} + C_3 \sqrt{2(\cos \psi_2 + \cos \phi_1)} - \frac{B_3 r_2 \sin \psi_2}{\sqrt{2(\cos \psi_2 + \cos \phi_1)}} \right] + \frac{1}{2} r_1 \sin \frac{\psi_1}{2}, \\
D_4 &= m \left[2 \cos \frac{\psi_1}{2} + C_4 \sqrt{2(\cos \psi_2 + \cos \phi_1)} \right] - \cos \frac{\psi_1}{2}, \\
D_5 &= n \left[r_2 \cos \frac{\phi_1}{2} + 2C_1 \sin \frac{\phi_1}{2} \right], \quad D_6 = 2nC_2 \sin \frac{\phi_1}{2}, \quad D_7 = 2nC_3 \sin \frac{\phi_1}{2}, \quad D_8 = 2nC_4 \sin \frac{\phi_1}{2}, \\
D_9 &= 0, \quad D_{10} = 0, \quad D_{11} = r_1 \cos \frac{\psi_1}{2}, \quad D_{12} = 2 \sin \frac{\psi_1}{2}.
\end{aligned} \tag{14}$$

Under the uniaxial tension loading (F), the total energy of the $1H\text{-}MX_2$ -[m, n] with the nonperiodic boundary can be expressed as

$$U = E_{\text{inner}} + E_{\text{bound}} - F dL,$$

$$\begin{aligned}
E_{\text{inner}} &= N \left[2K_r (dr_1^2 + 2dr_2^2) + 2(K_\phi + K_\theta) (d\phi_1^2 + 2d\phi_2^2) + K_\psi (d\psi_1^2 + 2d\psi_2^2) \right], \\
E_{\text{bound}} &= (m - n - 1)K_r dr_1^2 - (K_\phi + K_\theta) (md\phi_1^2 + 2nd\phi_2^2) + \frac{m - n - 1}{2} K_\psi d\psi_1^2,
\end{aligned} \tag{15}$$

where $N = m \times n$, $dL = dL_a$, and $dL = dL_z$ are the changes of sizes along the armchair and zigzag directions, respectively. E_{bound} is obtained by calculating the contributions from the effective bond lengths and bond angles (without dangling bonds) of the boundary. In conjunction with Eqs. (8), (10), and (13), the equilibrium equation can be expressed by four variables ($d\phi_1$, $d\phi_2$, $d\psi_1$, and dr_1) based on the principle of minimum potential energy ($\delta U = 0$),

$$\begin{bmatrix} K_{11} & K_{12} & K_{13} & K_{14} \\ K_{21} & K_{22} & K_{23} & K_{24} \\ K_{31} & K_{32} & K_{33} & K_{34} \\ K_{41} & K_{42} & K_{43} & K_{44} \end{bmatrix} \begin{bmatrix} d\phi_1 \\ d\phi_2 \\ d\psi_1 \\ dr_1 \end{bmatrix} = \begin{bmatrix} M_1 \\ M_2 \\ M_3 \\ M_4 \end{bmatrix}, \tag{16}$$

where

$$\begin{aligned}
K_{11} &= 2(2N - m)(K_\phi + K_\theta) + 8NK_r C_1^2 + 4NK_\psi B_1^2, \\
K_{12} &= K_{21} = 8NK_r C_1 C_2 + 4NK_\psi B_1 B_2, \\
K_{13} &= K_{31} = 8NK_r C_1 C_3 + 4NK_\psi B_1 B_3, \\
K_{14} &= K_{41} = 8NK_r C_1 C_4, \\
K_{22} &= 4(2N - n)(K_\phi + K_\theta) + 4N(2K_r C_2^2 + K_\psi B_2^2), \\
K_{23} &= K_{32} = 8NK_r C_2 C_3 + 4NK_\psi B_2 B_3, \\
K_{24} &= K_{42} = 8NK_r C_2 C_4, \\
K_{33} &= (2N + m - n - 1)K_\psi + 4N(2K_r C_3^2 + K_\psi B_3^2), \\
K_{34} &= K_{43} = 8NK_r C_3 C_4, \\
K_{44} &= 4NK_r (1 + 2C_4^2) + 2(m - n - 1)K_r.
\end{aligned} \tag{17}$$

For the tensile loading along the armchair direction,

$$M_1 = FD_1, M_2 = FD_2, M_3 = FD_3, M_4 = FD_4. \tag{18}$$

For the tensile loading along the zigzag direction,

$$M_1 = FD_5, M_2 = FD_6, M_3 = FD_7, M_4 = FD_8. \tag{19}$$

According to the above equations, the strains (ε) of $1H\text{-}MX_2$ along three different directions are

$$\begin{aligned}
\varepsilon_a &= \frac{dL_a}{L_a} = \frac{D_1 d\phi_1 + D_2 d\phi_2 + D_3 d\psi_1 + D_4 dr_1}{L_a}, \\
\varepsilon_z &= \frac{dL_z}{L_z} = \frac{D_5 d\phi_1 + D_6 d\phi_2 + D_7 d\psi_1 + D_8 dr_1}{L_z}, \\
\varepsilon_h &= \frac{dL_h}{L_h} = \frac{D_9 d\phi_1 + D_{10} d\phi_2 + D_{11} d\psi_1 + D_{12} dr_1}{L_h}.
\end{aligned} \tag{20}$$

The surface elastic moduli (E) of $1H\text{-}MX_2$ along the armchair and zigzag directions are expressed as

$$\begin{aligned}
E_a &= \frac{F}{L_z \varepsilon_a} = \frac{FL_a}{L_z (D_1 d\phi_1 + D_2 d\phi_2 + D_3 d\psi_1 + D_4 dr_1)}, \\
E_z &= \frac{F}{L_a \varepsilon_z} = \frac{FL_z}{L_a (D_5 d\phi_1 + D_6 d\phi_2 + D_7 d\psi_1 + D_8 dr_1)}.
\end{aligned} \tag{21}$$

The in-plane and out-of-plane Poisson's ratios (v_i and v_o) represent the ratios of in-plane and out-of-plane transverse strain to the longitudinal strain, respectively. Here, v_i and v_o of $1H\text{-}MX_2$ along the armchair and zigzag directions can be written as

$$\begin{aligned}
v_{ia} &= -\frac{\varepsilon_z}{\varepsilon_a} = -\frac{L_a (D_5 d\phi_1 + D_6 d\phi_2 + D_7 d\psi_1 + D_8 dr_1)}{L_z (D_1 d\phi_1 + D_2 d\phi_2 + D_3 d\psi_1 + D_4 dr_1)}, \\
v_{iz} &= -\frac{\varepsilon_a}{\varepsilon_z} = -\frac{L_z (D_1 d\phi_1 + D_2 d\phi_2 + D_3 d\psi_1 + D_4 dr_1)}{L_a (D_5 d\phi_1 + D_6 d\phi_2 + D_7 d\psi_1 + D_8 dr_1)}, \\
v_{oa} &= -\frac{\varepsilon_h}{\varepsilon_a} = -\frac{L_a (D_9 d\phi_1 + D_{10} d\phi_2 + D_{11} d\psi_1 + D_{12} dr_1)}{L_h (D_1 d\phi_1 + D_2 d\phi_2 + D_3 d\psi_1 + D_4 dr_1)}, \\
v_{oz} &= -\frac{\varepsilon_h}{\varepsilon_z} = -\frac{L_z (D_9 d\phi_1 + D_{10} d\phi_2 + D_{11} d\psi_1 + D_{12} dr_1)}{L_h (D_5 d\phi_1 + D_6 d\phi_2 + D_7 d\psi_1 + D_8 dr_1)}.
\end{aligned} \tag{22}$$

It is notable that as m and n tend to infinity, the expressions of the surface elastic modulus and in-plane and out-of-plane Poisson's ratios [see Eqs. (21) and (22)] along the two chiral directions will tend to be uniform. These limiting results can

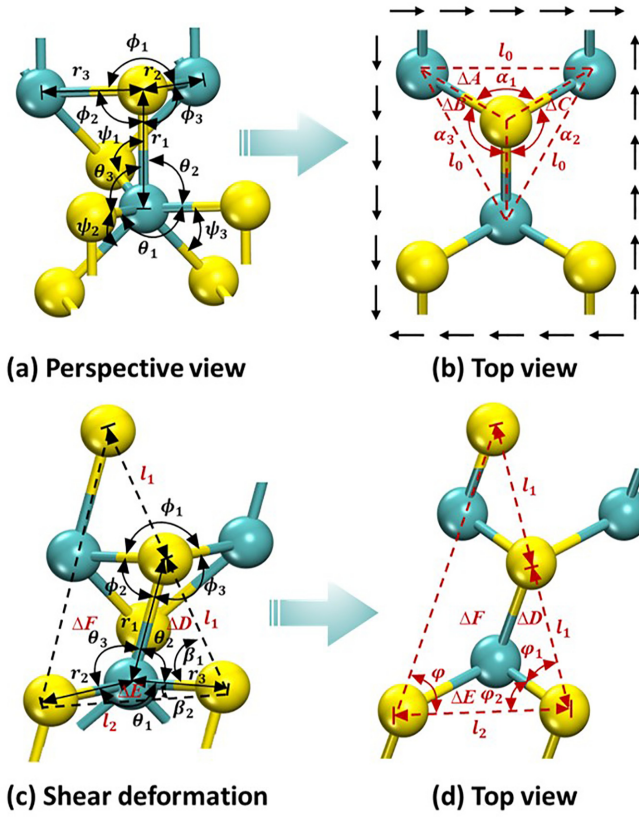


FIG. 3. The distribution of different types of bond lengths and bond angles under the shear deformation. The black arrows represent the directions of the loadings. The red and black dashed lines are auxiliary lines that characterize the geometrical relationships.

also be achieved by considering only the energy terms of inner unit cells (E_{inner}) without taking into account that of the boundary unit cells (E_{bound}).

C. Shear model

Under the loading of pure shear, the deformation of the unit cell can be characterized by three groups of variables (r_i , ϕ_i ,

θ_i , and ψ_i , where $\phi_i = \theta_i$, $i = 1, 2, 3$), as depicted in Fig. 3(a). To facilitate the construction of geometrical relationships and total energy expressions, we establish the corresponding auxiliary configurations, as shown in Figs. 3(b)–3(d). According to the consistency of thickness, the relationship between r_i and ψ_i is expressed as

$$r_1 \sin \frac{\psi_1}{2} = r_2 \sin \frac{\psi_2}{2} = r_3 \sin \frac{\psi_3}{2}. \quad (23)$$

Differentiating Eq. (23) leads to

$$\begin{aligned} dr_2 &= a_1 d\psi_1 + a_2 d\psi_2 + a_3 dr_1, \\ dr_3 &= a_4 d\psi_1 + a_5 d\psi_3 + a_6 dr_1, \end{aligned} \quad (24)$$

where

$$\begin{aligned} a_1 &= \frac{r_1 \cos \frac{\psi_1}{2}}{2 \sin \frac{\psi_2}{2}}, a_2 = -\frac{r_2 \cot \frac{\psi_2}{2}}{2}, a_3 = \frac{\sin \frac{\psi_1}{2}}{\sin \frac{\psi_2}{2}}, \\ a_4 &= \frac{r_1 \cos \frac{\psi_1}{2}}{2 \sin \frac{\psi_3}{2}}, a_5 = -\frac{r_3 \cot \frac{\psi_3}{2}}{2}, a_6 = \frac{\sin \frac{\psi_1}{2}}{\sin \frac{\psi_3}{2}}. \end{aligned} \quad (25)$$

According to the geometrical relationships in the triangles ΔA , ΔB , and ΔC [see Fig. 3(b)], the distance l_0 between adjacent M atoms can be written as

$$\begin{aligned} l_0 &= \left(r_2 \cos \frac{\psi_2}{2} \right)^2 + \left(r_3 \cos \frac{\psi_3}{2} \right)^2 \\ &\quad - 2r_2 r_3 \cos \frac{\psi_2}{2} \cos \frac{\psi_3}{2} \cos \alpha_1, \\ l_0 &= \left(r_1 \cos \frac{\psi_1}{2} \right)^2 + \left(r_2 \cos \frac{\psi_2}{2} \right)^2 \\ &\quad - 2r_1 r_2 \cos \frac{\psi_1}{2} \cos \frac{\psi_2}{2} \cos \alpha_2, \\ l_0 &= \left(r_1 \cos \frac{\psi_1}{2} \right)^2 + \left(r_3 \cos \frac{\psi_3}{2} \right)^2 \\ &\quad - 2r_1 r_3 \cos \frac{\psi_1}{2} \cos \frac{\psi_3}{2} \cos \alpha_3. \end{aligned} \quad (26)$$

In combination with Eq. (23), and then differentiating both sides of Eq. (26),

$$d\alpha_1 = b_1 d\psi_2 + b_2 d\psi_3 + b_3 d\phi_1, \quad d\alpha_2 = b_4 d\psi_3 + b_5 d\psi_1 + b_6 d\phi_2, \quad d\alpha_3 = b_7 d\psi_1 + b_8 d\psi_2 + b_9 d\phi_3, \quad (27)$$

where

$$\begin{aligned} b_1 &= \frac{\cos \frac{\psi_2}{2} \sin \frac{\psi_3}{2} - \sin \frac{\psi_2}{2} \cos \frac{\psi_3}{2} \cos \alpha_1}{2 \cos \frac{\psi_2}{2} \cos \frac{\psi_3}{2} \sin \alpha_1}, b_2 = \frac{\sin \frac{\psi_2}{2} \cos \frac{\psi_3}{2} - \cos \frac{\psi_2}{2} \sin \frac{\psi_3}{2} \cos \alpha_1}{2 \cos \frac{\psi_2}{2} \cos \frac{\psi_3}{2} \sin \alpha_1}, \\ b_4 &= \frac{\cos \frac{\psi_3}{2} \sin \frac{\psi_1}{2} - \sin \frac{\psi_3}{2} \cos \frac{\psi_1}{2} \cos \alpha_2}{2 \cos \frac{\psi_3}{2} \cos \frac{\psi_1}{2} \sin \alpha_2}, b_5 = \frac{\sin \frac{\psi_3}{2} \cos \frac{\psi_1}{2} - \cos \frac{\psi_3}{2} \sin \frac{\psi_1}{2} \cos \alpha_2}{2 \cos \frac{\psi_3}{2} \cos \frac{\psi_1}{2} \sin \alpha_2}, \\ b_7 &= \frac{\cos \frac{\psi_1}{2} \sin \frac{\psi_2}{2} - \sin \frac{\psi_1}{2} \cos \frac{\psi_2}{2} \cos \alpha_3}{2 \cos \frac{\psi_1}{2} \cos \frac{\psi_2}{2} \sin \alpha_3}, b_8 = \frac{\sin \frac{\psi_1}{2} \cos \frac{\psi_2}{2} - \cos \frac{\psi_1}{2} \sin \frac{\psi_2}{2} \cos \alpha_3}{2 \cos \frac{\psi_1}{2} \cos \frac{\psi_2}{2} \sin \alpha_3}, \\ b_3 &= \frac{\sin \phi_1}{\cos \frac{\psi_2}{2} \cos \frac{\psi_3}{2} \sin \alpha_1}, b_6 = \frac{\sin \phi_2}{\cos \frac{\psi_3}{2} \cos \frac{\psi_1}{2} \sin \alpha_2}, b_9 = \frac{\sin \phi_3}{\cos \frac{\psi_1}{2} \cos \frac{\psi_2}{2} \sin \alpha_3}. \end{aligned} \quad (28)$$

In the top view of the unit cell [see Fig. 3(b)], the angle variables satisfy $\alpha_1 + \alpha_2 + \alpha_3 = 2\pi$, thus, Eq. (27) can be reduced to

$$d\phi_3 = c_1 d\psi_1 + c_2 d\psi_2 + c_3 d\psi_3 + c_4 d\phi_1 + c_5 d\phi_2, \quad (29)$$

where

$$c_1 = -\frac{b_5 + b_7}{b_9}, \quad c_2 = -\frac{b_1 + b_8}{b_9}, \quad c_3 = -\frac{b_2 + b_4}{b_9}, \quad c_4 = -\frac{b_3}{b_9}, \quad c_5 = -\frac{b_6}{b_9}. \quad (30)$$

For the shear deformation [see Fig. 3(c)], the relationships of geometrical variables in the triangles ΔD and ΔE should satisfy

$$\frac{r_1}{\sin \beta_1} = \frac{r_3}{\sin(\beta_1 + \theta_2)} = \frac{r_3}{\sin(\beta_1 + \phi_2)}, \quad \frac{r_2}{\sin \beta_2} = \frac{r_3}{\sin(\beta_2 + \theta_1)} = \frac{r_3}{\sin(\beta_2 + \phi_1)}. \quad (31)$$

Substituting Eq. (23) into Eq. (31),

$$\sin \frac{\psi_1}{2} \sin \beta_1 = \sin \frac{\psi_3}{2} \sin(\beta_1 + \phi_2), \quad \sin \frac{\psi_2}{2} \sin \beta_2 = \sin \frac{\psi_3}{2} \sin(\beta_2 + \phi_1). \quad (32)$$

Expanding both sides of Eq. (32) leads to

$$V_1 \sin \beta_1 - V_2 \cos \beta_1 = V \sin(\beta_1 - \delta_1) = 0, \quad Q_1 \sin \beta_2 - Q_2 \cos \beta_2 = Q \sin(\beta_2 - \delta_2) = 0, \quad (33)$$

where

$$V_1 = \sin \frac{\psi_1}{2} - \sin \frac{\psi_3}{2} \cos \phi_2, \quad V_2 = \sin \frac{\psi_3}{2} \sin \phi_2, \quad V = \sqrt{V_1^2 + V_2^2}, \quad \tan \delta_1 = \frac{V_2}{V_1}, \quad \beta_1 = |\delta_1|, \\ Q_1 = \sin \frac{\psi_2}{2} - \sin \frac{\psi_3}{2} \cos \phi_1, \quad Q_2 = \sin \frac{\psi_3}{2} \sin \phi_1, \quad Q = \sqrt{Q_1^2 + Q_2^2}, \quad \tan \delta_2 = \frac{Q_2}{Q_1}, \quad \beta_2 = |\delta_2|. \quad (34)$$

Then, differentiating both sides of Eq. (32),

$$d\beta_1 = d_1 d\psi_1 + d_2 d\psi_3 + d_3 d\phi_2, \quad d\beta_2 = d_4 d\psi_2 + d_5 d\psi_3 + d_6 d\phi_1, \quad (35)$$

where

$$d_1 = \frac{-\cos \frac{\psi_1}{2} \sin \beta_1}{2[\sin \frac{\psi_1}{2} \cos \beta_1 - \sin \frac{\psi_3}{2} \cos(\beta_1 + \phi_2)]}, \quad d_2 = \frac{\cos \frac{\psi_3}{2} \sin(\beta_1 + \phi_2)}{2[\sin \frac{\psi_1}{2} \cos \beta_1 - \sin \frac{\psi_3}{2} \cos(\beta_1 + \phi_2)]}, \\ d_3 = \frac{\sin \frac{\psi_3}{2} \cos(\beta_1 + \phi_2)}{\sin \frac{\psi_1}{2} \cos \beta_1 - \sin \frac{\psi_3}{2} \cos(\beta_1 + \phi_2)}, \quad d_4 = \frac{-\cos \frac{\psi_2}{2} \sin \beta_2}{2[\sin \frac{\psi_2}{2} \cos \beta_2 - \sin \frac{\psi_3}{2} \cos(\beta_2 + \phi_1)]}, \\ d_5 = \frac{\cos \frac{\psi_3}{2} \sin(\beta_2 + \phi_1)}{2[\sin \frac{\psi_2}{2} \cos \beta_2 - \sin \frac{\psi_3}{2} \cos(\beta_2 + \phi_1)]}, \quad d_6 = \frac{\sin \frac{\psi_3}{2} \cos(\beta_2 + \phi_1)}{\sin \frac{\psi_2}{2} \cos \beta_2 - \sin \frac{\psi_3}{2} \cos(\beta_2 + \phi_1)}. \quad (36)$$

The shear deformation of the unit cell can be characterized by the angle variable (φ), as depicted in Fig. 3(d). Based on the geometrical relationships, the corresponding angle variables in the triangles ΔD and ΔE satisfy the following equations:

$$\cos \beta_1 = \cos \frac{\psi_3}{2} \cos \varphi_1, \quad \cos \beta_2 = \cos \frac{\psi_3}{2} \cos \varphi_2. \quad (37)$$

Differencing Eq. (37) leads to

$$d\varphi_1 = e_1 d\psi_3 + e_2 d\beta_1, \quad d\varphi_2 = e_3 d\psi_3 + e_4 d\beta_2, \quad (38)$$

where

$$e_1 = -\frac{\sin \frac{\psi_3}{2} \cos \varphi_1}{2 \cos \frac{\psi_3}{2} \sin \varphi_1}, \quad e_2 = \frac{\sin \beta_1}{\cos \frac{\psi_3}{2} \sin \varphi_1}, \\ e_3 = -\frac{\sin \frac{\psi_3}{2} \cos \varphi_2}{2 \cos \frac{\psi_3}{2} \sin \varphi_2}, \quad e_4 = \frac{\sin \beta_2}{\cos \frac{\psi_3}{2} \sin \varphi_2}. \quad (39)$$

In addition, the relationship of the angle variables (φ , φ_1 , and φ_2) in the triangle ΔF satisfy

$$\frac{2l_1}{\sin \varphi} = \frac{l_2}{\sin(\varphi + \varphi_1 + \varphi_2)}. \quad (40)$$

Substituting Eqs. (23) and (31) into Eq. (40) leads to

$$\sin(\beta_1 + \phi_2) \sin \phi_1 \sin \varphi \\ = 2 \sin(\beta_2 + \phi_1) \sin \phi_2 \sin(\varphi + \varphi_1 + \varphi_2). \quad (41)$$

Expanding both sides of Eq. (41),

$$R_1 \sin \varphi - R_2 \cos \varphi = R \sin(\varphi - \delta_3) = 0, \quad (42)$$

where

$$R_1 = \sin(\beta_1 + \phi_2) \sin \phi_1 - 2 \sin(\beta_2 + \phi_1) \sin \phi_2 \cos(\varphi_1 + \varphi_2),$$

$$R_2 = 2 \sin(\beta_2 + \phi_1) \sin \phi_2 \sin(\varphi_1 + \varphi_2),$$

$$R = \sqrt{R_1^2 + R_2^2}, \quad \tan \delta_3 = \frac{R_2}{R_1}, \quad \varphi = |\delta_3|. \quad (43)$$

Differencing both the sides of Eq. (41),

$$d\varphi = f_1 d\phi_1 + f_2 d\phi_2 + f_3 d\beta_1 + f_4 d\beta_2 + f_5 d\varphi_1 + f_6 d\varphi_2, \quad (44)$$

where

$$\begin{aligned} f_1 &= \frac{2 \cos(\beta_2 + \phi_1) \sin \phi_2 \sin(\varphi + \varphi_1 + \varphi_2) - \sin(\beta_1 + \phi_2) \cos \phi_1 \sin \varphi}{\sin(\beta_1 + \phi_2) \sin \phi_1 \cos \varphi - 2 \sin(\beta_2 + \phi_1) \sin \phi_2 \cos(\varphi + \varphi_1 + \varphi_2)}, \\ f_2 &= \frac{2 \sin(\beta_2 + \phi_1) \cos \phi_2 \sin(\varphi + \varphi_1 + \varphi_2) - \cos(\beta_1 + \phi_2) \sin \phi_1 \sin \varphi}{\sin(\beta_1 + \phi_2) \sin \phi_1 \cos \varphi - 2 \sin(\beta_2 + \phi_1) \sin \phi_2 \cos(\varphi + \varphi_1 + \varphi_2)}, \\ f_3 &= \frac{-\cos(\beta_1 + \phi_2) \sin \phi_1 \sin \varphi}{\sin(\beta_1 + \phi_2) \sin \phi_1 \cos \varphi - 2 \sin(\beta_2 + \phi_1) \sin \phi_2 \cos(\varphi + \varphi_1 + \varphi_2)}, \\ f_4 &= \frac{2 \cos(\beta_2 + \phi_1) \sin \phi_2 \sin(\varphi + \varphi_1 + \varphi_2)}{\sin(\beta_1 + \phi_2) \sin \phi_1 \cos \varphi - 2 \sin(\beta_2 + \phi_1) \sin \phi_2 \cos(\varphi + \varphi_1 + \varphi_2)}, \\ f_5 &= f_6 = \frac{2 \sin(\beta_2 + \phi_1) \sin \phi_2 \cos(\varphi + \varphi_1 + \varphi_2)}{\sin(\beta_1 + \phi_2) \sin \phi_1 \cos \varphi - 2 \sin(\beta_2 + \phi_1) \sin \phi_2 \cos(\varphi + \varphi_1 + \varphi_2)}. \end{aligned} \quad (45)$$

In conjunction with Eqs. (35) and (38), the shear strain ($d\varphi$) can be expressed by the variables of $d\psi_1$, $d\psi_2$, $d\psi_3$, $d\phi_1$, and $d\phi_2$,

$$d\varphi = g_1 d\psi_1 + g_2 d\psi_2 + g_3 d\psi_3 + g_4 d\phi_1 + g_5 d\phi_2, \quad (46)$$

where

$$\begin{aligned} g_1 &= (f_3 + e_2 f_5) d_1, \quad g_2 = (f_4 + e_4 f_6) d_4, \\ g_3 &= e_1 f_5 + e_3 f_6 + (f_3 + e_2 f_5) d_2 + (f_4 + e_4 f_6) d_5, \\ g_4 &= f_1 + (f_4 + e_4 f_6) d_6, \quad g_5 = f_2 + (f_3 + e_2 f_5) d_3. \end{aligned} \quad (47)$$

Under the pure shear loading, the total energy of the $1H-MX_2-[m, n]$ with the nonperiodic boundary is written as

$$\begin{aligned} U &= E_{\text{inner}} + E_{\text{bound}} - T d\varphi, \\ E_{\text{inner}} &= N[2K_r(dr_1^2 + dr_2^2 + dr_3^2) + 2(K_\phi + K_\theta)(d\phi_1^2 + d\phi_2^2 + d\phi_3^2) + K_\psi(d\psi_1^2 + d\psi_2^2 + d\psi_3^2)], \\ E_{\text{bound}} &= (m - n - 1)K_r dr_1^2 - (K_\phi + K_\theta)(md\phi_1^2 + nd\phi_2^2 + nd\phi_3^2) + \frac{m - n - 1}{2}K_\psi d\psi_1^2, \end{aligned} \quad (48)$$

where $T = \tau L_a L_z$ represents the moment of force and τ is the shear loading. In conjunction with Eqs. (24), (29), and (46), the equilibrium equation can be expressed by six variables ($d\psi_1$, $d\psi_2$, $d\psi_3$, $d\phi_1$, $d\phi_2$, and dr_1) based on the principle of minimum potential energy ($\delta U = 0$),

$$\begin{bmatrix} P_{11} & P_{12} & P_{13} & P_{14} & P_{15} & P_{16} \\ P_{21} & P_{22} & P_{23} & P_{24} & P_{25} & P_{26} \\ P_{31} & P_{32} & P_{33} & P_{34} & P_{35} & P_{36} \\ P_{41} & P_{42} & P_{43} & P_{44} & P_{45} & P_{46} \\ P_{51} & P_{52} & P_{53} & P_{54} & P_{55} & P_{56} \\ P_{61} & P_{62} & P_{63} & P_{64} & P_{65} & P_{66} \end{bmatrix} \begin{bmatrix} d\psi_1 \\ d\psi_2 \\ d\psi_3 \\ d\phi_1 \\ d\phi_2 \\ dr_1 \end{bmatrix} = \begin{bmatrix} H_1 \\ H_2 \\ H_3 \\ H_4 \\ H_5 \\ H_6 \end{bmatrix}, \quad (49)$$

where

$$\begin{aligned} P_{11} &= (2N + m - n - 1)K_\psi + 4NK_r(a_1^2 + a_4^2) + 2(2N - n)(K_\phi + K_\theta)c_1^2, \\ P_{12} &= P_{21} = 4NK_r a_1 a_2 + 2(2N - n)(K_\phi + K_\theta)c_1 c_2, \\ P_{13} &= P_{31} = 4NK_r a_4 a_5 + 2(2N - n)(K_\phi + K_\theta)c_1 c_3, \\ P_{14} &= P_{41} = 2(2N - n)(K_\phi + K_\theta)c_1 c_4, \quad P_{15} = P_{51} = 2(2N - n)(K_\phi + K_\theta)c_1 c_5, \\ P_{16} &= P_{61} = 4NK_r(a_1 a_3 + a_4 a_6), \\ P_{22} &= 2NK_\psi + 4NK_r a_2^2 + 2(2N - n)(K_\phi + K_\theta)c_2^2, \\ P_{23} &= P_{32} = 2(2N - n)(K_\phi + K_\theta)c_2 c_3, \quad P_{24} = P_{42} = 2(2N - n)(K_\phi + K_\theta)c_2 c_4, \\ P_{25} &= P_{52} = 2(2N - n)(K_\phi + K_\theta)c_2 c_5, \quad P_{26} = P_{62} = 4NK_r a_2 a_3, \end{aligned}$$

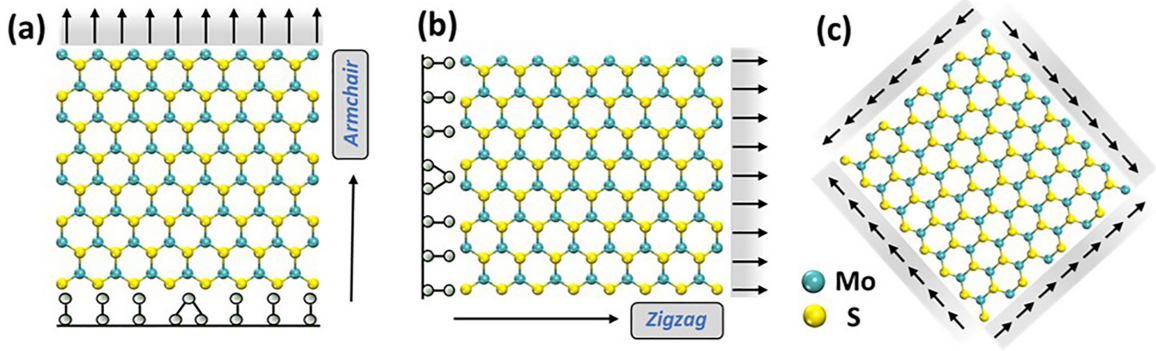


FIG. 4. The constrained conditions of the 1H-MoS₂ in MD simulations. Panels (a) and (b) show the cases of uniaxial tension along the armchair and zigzag directions, respectively. (c) The case of pure shear. The arrows represent the directions of the loadings.

$$\begin{aligned}
 P_{33} &= 2NK_\psi + 4NK_r a_5^2 + 2(2N - n)(K_\phi + K_\theta)c_3^2, \\
 P_{34} &= P_{43} = 2(2N - n)(K_\phi + K_\theta)c_3c_4, \quad P_{35} = P_{53} = 2(2N - n)(K_\phi + K_\theta)c_3c_5, \\
 P_{36} &= P_{63} = 4NK_r a_5a_6, \quad P_{44} = 2(K_\phi + K_\theta)[(2N - m) + (2N - n)c_4^2], \\
 P_{45} &= P_{54} = 2(2N - n)(K_\phi + K_\theta)c_4c_5, \\
 P_{46} &= P_{64} = 0, \quad P_{55} = 2(2N - n)(K_\phi + K_\theta)(1 + c_5^2), \quad P_{56} = P_{65} = 0, \\
 P_{66} &= 4NK_r(1 + a_3^2 + a_6^2) + 2(m - n - 1)K_r, \\
 H_1 &= Tg_1, H_2 = Tg_2, H_3 = Tg_3, H_4 = Tg_4, H_5 = Tg_5, H_6 = 0.
 \end{aligned} \tag{50}$$

According to the above equations, the surface shear modulus (G) of 1H-MX₂ can be written as

$$G = \frac{T}{L_a L_z d\varphi} = \frac{T}{L_a L_z (g_1 d\psi_1 + g_2 d\psi_2 + g_3 d\psi_3 + g_4 d\phi_1 + g_5 d\phi_2)}. \tag{51}$$

For the 1H-MX₂ with periodic boundary, the expression of surface shear modulus can be obtained by considering only the energy terms of inner unit cells (E_{inner}) and ignoring the energy term of boundary unit cells (E_{bound}). It should be noted that this expression will also be consistent with Eq. (51) when the number of unit cells tends to infinity (i.e., $m \rightarrow \infty$ and $n \rightarrow \infty$).

III. RESULTS AND DISCUSSION

A. Validation by MD simulations

To validate the validity and correctness of the proposed analytical algorithm (theoretical model), the mechanical behaviors of the 1H-MoS₂ are examined by MD simulations. The simulations are carried out in the LAMMPS software. The geometrical structure and force-constant parameters of 1H-MoS₂ are consistent with the established theoretical model and based on the previous works [37,38]. The MD simulations with nonperiodic boundary conditions are performed within the NVT ensemble by the Nosé-Hoover thermostat. The time step is 1 fs. Since the intrinsic mechanical properties are examined in the MM theoretical model (without the effect of temperature), the system temperature of MD simulations is set to 0.01 K to eliminate the effect of temperature as much as possible.

The computational configurations of 1H-MoS₂ under the uniaxial tension and pure shear loadings are depicted in Fig. 4.

For the tensile simulations, one side of MoS₂ is fixed (the three directions of one atom in the middle position of the constrained boundary is fixed, while the other atoms on this boundary are constrained only in the tensile direction), and the other is subjected to stretch. The constraints and loadings are applied along the armchair and zigzag directions to examine the chirality dependence, respectively. As for the shear simulations, two mutually perpendicular loadings are applied to boundary atoms to form the pure shear condition. The computational results are statistically analyzed within the small deformations. Here, the maximum tension and shear strain are 0.02 and 0.03, respectively. Moreover, to further investigate the size-dependent mechanical properties of MoS₂, the square models with sizes ranging from 3 nm × 3 nm to 50 nm × 50 nm are constructed in this section.

B. Size and chirality dependence of 1H-MoS₂

The variations of four mechanical properties of 1H-MoS₂ with the size of boundary are discussed in this section, as depicted in Fig. 5. It can be seen that the computational results of the MM method are in good agreement with those of the MD simulation. The average errors of the surface elastic modulus (E), surface shear modulus (G), and in-plane and out-of-plane Poisson's ratios (ν_i and ν_o) between the MM and MD results are about 0.19%, 0.24%, 1.01%, and 3.91%, respectively. Notably, the mechanical properties of MoS₂ present significant

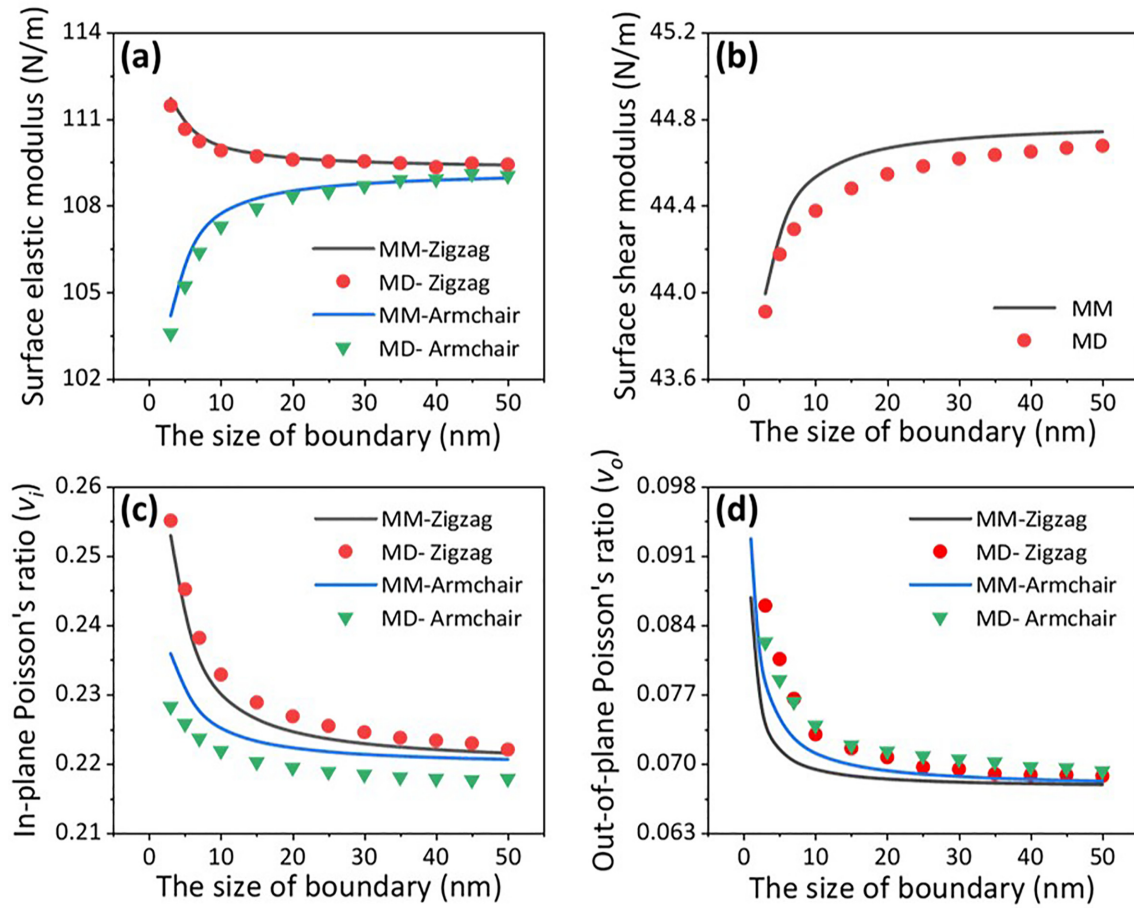


FIG. 5. The variation of mechanical properties of 1H-MoS₂ with the size of boundary. (a) Surface elastic modulus. (b) Surface shear modulus. (c) In-plane Poisson's ratio. (d) Out-of-plane Poisson's ratio.

size and chirality dependence. From Fig. 5(a), it is found that the surface elastic modulus displays an opposite variation tendency along different chiral directions with increasing size. This opposite trend is also observed and validated in previous works on the elastic modulus and bending stiffness of graphene and MoS₂ [32,39,40]. As the size increases, the surface elastic moduli along the two directions gradually approach the same value ($E = 109.25$ N/m). For the surface shear modulus, it also exhibits a notable size dependence. With the increase in size, the surface shear modulus increases gradually and tends to be stable ($G = 44.79$ N/m). As for the in-plane and out-of-plane Poisson's ratios, they decrease and gradually converge ($\nu_i = 0.22$ and $\nu_o = 0.07$) with increasing size [see Figs. 5(c) and 5(d)]. The above results are close to the existing experimental and numerical works ($E = 90.0$ – 124.5 N/m, $\nu_i = 0.21$ – 0.25 , $G = 36.1$ – 48.6 N/m) [21,25,41–43], which verifies the correctness of the proposed theoretical model.

Moreover, the computational results indicate that the mechanical properties of small-sized MoS₂ show an obvious size and chirality-dependence, and these properties tend to be stable gradually when the size exceeds 20 nm. This is because the boundary unit cell (E_{bound}) occupies a large proportion and plays an important role in small-sized materials. As the size increases, the proportion of E_{bound} decreases gradually and

the role of the stable inner unit cell (E_{inner}) becomes more and more dominant. Thus, the mechanical properties of MoS₂ tend to be stable and uniform.

C. Mechanical properties of 34 types of 1H-MX₂

Based on the constructed theoretical model, we predict four mechanical properties of 34 1H-MX₂ materials ($M = \text{Sc, Ti, V, Cr, Mn, Fe, Co, Ni, Nb, Mo, Ta, W; } X = \text{O, S, Se, Te}$) in this section. The geometrical structure and force-constant parameters involved in the theoretical models are based on previous studies [11,44]. Table I exhibits the calculated surface elastic and shear moduli and in-plane and out-of-plane Poisson's ratios of 34 1H-MX₂. In order to verify the validity of these results, several groups of the common and representative 1H-MX₂ ($M = \text{Cr, Mo, W; } X = \text{O, S, Se, Te}$) are selected for comparison. It can be seen that the computational results are in good agreement with the existing experimental, DFT, and MD results [22,25,29,43–48], which indicates that the proposed theoretical model can be widely used in 1H-MX₂.

For the M and X elements from different periods and groups, the formed 1H-MX₂ exhibits diverse mechanical performances. It is notable that the surface elastic and shear moduli of 1H-MX₂ usually decrease with X from O to Te under the same M element, which is mainly attributed to

TABLE I. The mechanical properties of 34 types of $1H-MX_2$.

Type	E (N/m)	Refs.	ν_i	Refs.	ν_o	G (N/m)	Refs.
ScO ₂	128.3		0.16		0.17	55.4	
ScS ₂	44.0		0.30		0.31	16.9	
ScSe ₂	39.9		0.32		0.31	15.1	
ScTe ₂	29.0		0.38		0.17	10.5	
TiTe ₂	47.9		0.29		0.12	18.6	
VO ₂	135.8		0.17		0.05	58.0	
VS ₂	86.7		0.28		0.12	33.9	
VSe ₂	82.4		0.23		0.06	33.4	
VTe ₂	68.1		0.28		0.10	26.7	
CrO ₂	214.2	209.0 ^a	0.13	0.13 ^a	-0.03	94.7	
CrS ₂	99.3	110.4 ^b	0.26	0.26 ^b	0.09	39.4	43.7 ^b
CrSe ₂	90.2	85.6 ^b	0.30	0.31 ^b	0.13	34.6	32.7 ^b
CrTe ₂	77.9	76.4 ^a	0.30	0.30 ^a	0.13	29.9	
MnO ₂	163.9		0.10		-0.04	74.4	
FeO ₂	101.7		0.23		0.11	41.4	
FeS ₂	85.1		0.20		0.06	35.4	
FeSe ₂	78.3		0.23		0.09	31.9	
FeTe ₂	70.6		0.25		0.12	28.2	
CoTe ₂	54.4		0.32		0.23	20.7	
NiS ₂	85.0		0.19		0.24	35.6	
NiSe ₂	48.3		0.27		0.19	19.0	
NiTe ₂	53.9		0.32		0.25	20.5	
NbS ₂	88.6		0.27		0.11	34.9	
NbSe ₂	81.2		0.29		0.13	31.5	
MoO ₂	214.3	209.3 ^a	0.17	0.17 ^a	0.03	91.6	103.6 ^c
MoS ₂	109.2	124.5 ^d	0.22	0.25 ^d	0.07	44.8	48.6 ^e
MoSe ₂	103.6	103.9 ^d	0.24	0.23 ^d	0.04	41.9	41.1 ^e
MoTe ₂	80.0	79.4 ^d	0.25	0.24 ^d	0.04	32.1	28.6 ^f
TaS ₂	87.8		0.27		0.11	34.5	
TaSe ₂	81.7		0.29		0.12	31.7	
WO ₂	242.4	237.2 ^a	0.15	0.15 ^a	0.00	105.7	131.5 ^c
WS ₂	123.2	139.5 ^g	0.21	0.22 ^g	0.02	50.8	58.1 ^h
WSe ₂	125.0	115.5 ^g	0.20	0.19 ^g	-0.01	52.2	49.2 ^h
WTe ₂	83.2	86.9 ^g	0.20	0.18 ^g	-0.01	34.8	30.5 ^f

^aReference [44].^bReference [45].^cReference [46].^dReference [25].^eReference [43].^fReference [47].^gReference [29].^hReference [48].

the reducing force-constant parameters of bond lengths and bond angles. This implies that the mechanical properties of the transition-metal dioxides and dichalcogenides decrease with the increase in the periods of chalcogens (two to five periods). Furthermore, the out-of-plane Poisson's ratio is one of the important properties to characterize the out-of-plane deformability of materials, however, few studies have paid attention to it. Here, we report the out-of-plane Poisson's ratio of 34 $1H-MX_2$ compounds. Interestingly, some of these materials show a negative out-of-plane Poisson's ratio (such as CrO₂, MnO₂, WSe₂, and WTe₂), which is a unique property and is also reported in some $1T-MX_2$ and black phosphorus [49,50]. The above findings will be beneficial in predicting the

mechanical performances of the potential materials and may shed light on the structural design of materials with a negative Poisson's ratio.

D. Effects of geometrical structure and force-constant parameters

In fact, the $1H-MX_2$ has a large number of members. Although the mechanical properties of 34 $1H-MX_2$ materials are given in Table I, there are still many materials that have not been examined. Besides, the geometrical structure and force-constant parameters of some $1H-MX_2$ materials are still not determined and reported in the existing research, making it difficult to obtain the mechanical properties of the relevant materials directly by computational methods. It is worth noting that for different $1H-MX_2$ materials, the molecular structures (bond lengths and bond angles) and force field parameters almost fall within a certain range. Therefore, the mechanical properties of the similar and unreported $1H-MX_2$ can be predicted by investigating the roles in the geometrical structure and force-constant parameters based on the proposed analytical algorithm.

Figure 6 illustrates the variation of four mechanical properties of $1H-MX_2$ with the scaling factor. Here, the scaling factor is defined as M_c/M_r , in which M_c and M_r are the concerned variables (the geometrical structure and force-constant parameters) of the current and reference configurations (customized configuration), respectively. The relevant parameters of the customized configuration of $1H-MX_2$ (the intersection of the curves) are listed in Table II. It should be noted that the effects of two groups of parameters (i.e., ϕ and θ , K_ϕ and K_θ) are identical due to the structural symmetry of $1H-MX_2$. The surface elastic and shear moduli increase with the force-constant parameters (K_r , K_ϕ , K_θ , and K_ψ). In-plane and out-of-plane Poisson's ratios increase with increasing K_r , however, they decrease with the angle-related force-constant parameters (K_ϕ and K_θ). Compared to the force-constant parameters, the geometrical structure parameters have a more significant effect on the mechanical properties. Here, the roles of three bond angles ϕ , θ , and ψ on the mechanical properties are generally consistent. Interestingly, as the bond length r increases, the surface elastic and shear moduli decrease, but the in-plane and out-of-plane Poisson's ratios increase. These results provide an essential reference for understanding the roles of molecular structures in mechanical performances and offer a feasible method for predicting the mechanical properties of unreported $1H-MX_2$ materials. Moreover, the proposed theoretical model can be utilized to construct a visual computational platform for rapid evaluation of the mechanical properties of $1H-MX_2$ materials, which will be of great significance for the application of the constructed theoretical model.

IV. CONCLUSIONS

This work proposes a MM theoretical model for the comprehensive, accurate, and rapid evaluation on the mechanical properties (surface elastic and shear moduli and in-plane and out-of-plane Poisson's ratios) of the $1H-MX_2$ family. Taking $1H-MoS_2$ as the concerned materials, the size and chirality dependence on the mechanical behaviors are examined, and

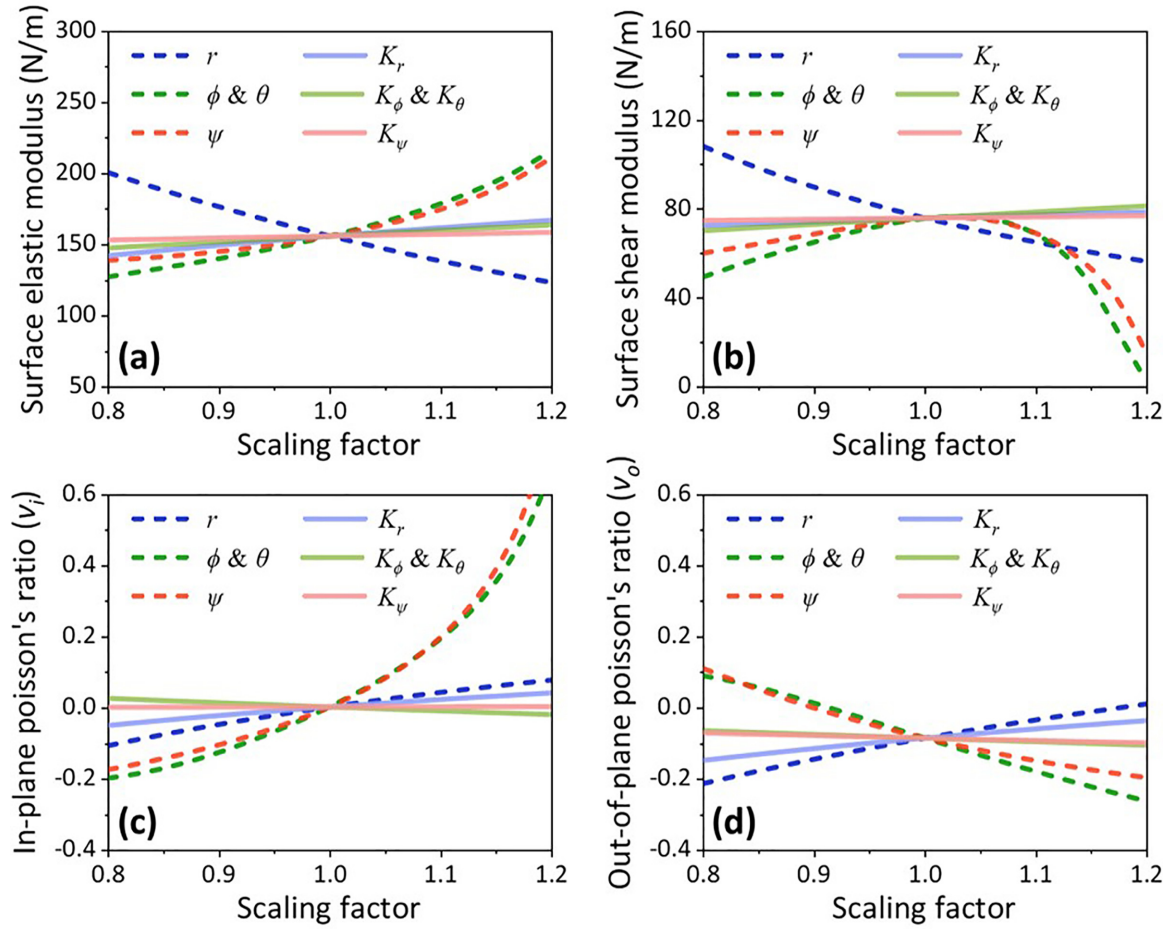


FIG. 6. The variation of four mechanical properties of $1H\text{-}MX_2$ with the geometrical structure and force-constant parameters. (a) Surface elastic modulus. (b) Surface shear modulus. (c) In-plane Poisson's ratio. (d) Out-of-plane Poisson's ratio.

MD simulations are utilized to verify the constructed theoretical model. It is worth noting that we present a library for the mechanical properties of 34 $1H\text{-}MX_2$ materials by utilizing the proposed method. The results indicate that the mechanical properties of $1H\text{-}MX_2$ depend on the period and group numbers of transition metals and chalcogens. Here, the surface elastic and shear moduli decrease with the increase of the chalcogen period, which is related to the cooperative contributions of geometrical structure and force-constant parameters. The relevant results are in good agreement with the existing experimental and numerical works. Furthermore, the relationships between the molecular structures (bond lengths and bond angles) and mechanical properties are elucidated, which provides a feasible way to predict the mechanical properties of unreported $1H\text{-}MX_2$. Interestingly, by considering interlayer interactions and different geometrical relationships,

the proposed theoretical model has great potential to characterize multilayer structures and other structural phases of MX_2 materials. The present findings offer an essential theoretical basis for understanding the nanostructures and properties of $1H\text{-}MX_2$, which could facilitate the design and fabrication of 2D materials-based nanodevices, microfluidic chips, etc.

ACKNOWLEDGMENTS

The support from the National Natural Science Foundation of China (Grants No. 12372192, No. 11972108, No. 12072061, and No. 12072062), the National Key R&D Program of China (Grant No. 2022YFB4201200), and Fundamental Research Funds for the Central Universities is gratefully acknowledged.

TABLE II. The geometrical structure and force-constant parameters of the reference configuration of $1H\text{-}MX_2$.

$r_{\text{Mo-S}} (\text{\AA})$	$\phi_{\text{MoSMo}} (^{\circ})$	$\theta_{\text{SMoS}} (^{\circ})$	$\psi_{\text{SMoS}} (^{\circ})$	$K_r (\text{eV}/\text{\AA}^2)$	$K_{\phi} (\text{eV})$	$K_{\theta} (\text{eV})$	$K_{\psi} (\text{eV})$
2.0	80.0	80.0	80.0	8.0	8.0	8.0	8.0

- [1] K. S. Novoselov, A. Mishchenko, A. Carvalho, and A. H. Castro Neto, 2D materials and van der Waals heterostructures, *Science* **353**, aac9439 (2016).
- [2] S. Manzeli, D. Ovchinnikov, D. Pasquier, O. V. Yazyev, and A. Kis, 2D transition metal dichalcogenides, *Nat. Rev. Mater.* **2**, 17033 (2017).
- [3] K. Cao, S. Feng, Y. Han, L. Gao, T. Hue Ly, Z. Xu, and Y. Lu, Elastic straining of free-standing monolayer graphene, *Nat. Commun.* **11**, 284 (2020).
- [4] Q. Lu and R. Huang, Excess energy and deformation along free edges of graphene nanoribbons, *Phys. Rev. B* **81**, 155410 (2010).
- [5] K. S. Novoselov, A. K. Geim, S. V. Morozov, D. Jiang, M. I. Katsnelson, I. V. Grigorieva, S. V. Dubonos, and A. A. Firsov, Two-dimensional gas of massless Dirac fermions in graphene, *Nature (London)* **438**, 197 (2005).
- [6] D. J. Late, B. Liu, H. S. S. R. Matte, V. P. Dravid, and C. N. R. Rao, Hysteresis in single-layer MoS₂ field effect transistors, *ACS Nano* **6**, 5635 (2012).
- [7] J. Li, H. Zhang, Z. Guo, J.-W. Jiang, and T. Chang, Thermal stability of twin graphene: A Reaxff molecular dynamics study, *Appl. Surf. Sci.* **623**, 157038 (2023).
- [8] M. Chhowalla, Z. Liu, and H. Zhang, Two-dimensional transition metal dichalcogenide (TMD) nanosheets, *Chem. Soc. Rev.* **44**, 2584 (2015).
- [9] T. Yang, T. T. Song, M. Callsen, J. Zhou, J. W. Chai, Y. P. Feng, S. J. Wang, and M. Yang, Atomically thin 2D transition metal oxides: Structural reconstruction, interaction with substrates, and potential applications, *Adv. Mater. Interfaces* **6**, 1801160 (2019).
- [10] M. Samadi, N. Sarikhani, M. Zirak, H. Zhang, H.-L. Zhang, and A. Z. Moshfegh, Group 6 transition metal dichalcogenide nanomaterials: Synthesis, applications and future perspectives, *Nanoscale Horiz.* **3**, 90 (2018).
- [11] C. Ataca, H. Şahin, and S. Ciraci, Stable, single-layer MX₂ transition-metal oxides and dichalcogenides in a honeycomb-like structure, *J. Phys. Chem. C* **116**, 8983 (2012).
- [12] X. Zhang, Q.-H. Tan, J.-B. Wu, W. Shi, and P.-H. Tan, Review on the Raman spectroscopy of different types of layered materials, *Nanoscale* **8**, 6435 (2016).
- [13] M. Yagmurcukardes and F. M. Peeters, Stable single layer of Janus MoSO: Strong out-of-plane piezoelectricity, *Phys. Rev. B* **101**, 155205 (2020).
- [14] M. Calandra, Chemically exfoliated single-layer MoS₂: Stability, lattice dynamics, and catalytic adsorption from first principles, *Phys. Rev. B* **88**, 245428 (2013).
- [15] A. Splendiani, L. Sun, Y. Zhang, T. Li, J. Kim, C.-Y. Chim, G. Galli, and F. Wang, Emerging photoluminescence in monolayer MoS₂, *Nano Lett.* **10**, 1271 (2010).
- [16] K. Kalantar-zadeh, J. Z. Ou, T. Daeneke, A. Mitchell, T. Sasaki, and M. S. Fuhrer, Two dimensional and layered transition metal oxides, *Appl. Mater. Today* **5**, 73 (2016).
- [17] K. F. Mak and J. Shan, Photonics and optoelectronics of 2D semiconductor transition metal dichalcogenides, *Nat. Photon.* **10**, 216 (2016).
- [18] Z. Dai, L. Liu, and Z. Zhang, Strain engineering of 2D materials: Issues and opportunities at the interface, *Adv. Mater.* **31**, 1805417 (2019).
- [19] K. He, C. Poole, K. F. Mak, and J. Shan, Experimental demonstration of continuous electronic structure tuning via strain in atomically thin MoS₂, *Nano Lett.* **13**, 2931 (2013).
- [20] H. Jiang, L. Zheng, Z. Liu, and X. Wang, Two-dimensional materials: From mechanical properties to flexible mechanical sensors, *InfoMat* **2**, 1077 (2020).
- [21] R. C. Cooper, C. Lee, C. A. Marianetti, X. Wei, J. Hone, and J. W. Kysar, Nonlinear elastic behavior of two-dimensional molybdenum disulfide, *Phys. Rev. B* **87**, 035423 (2013).
- [22] Y. Yang, X. Li, M. Wen, E. Hacıoğlu, W. Chen, Y. Gong, J. Zhang, B. Li, W. Zhou, P. M. Ajayan *et al.*, Brittle fracture of 2D MoSe₂, *Adv. Mater.* **29**, 1604201 (2017).
- [23] N. Iguñiz, R. Frisenda, R. Bratschkitsch, and A. Castellanos-Gomez, Revisiting the buckling metrology method to determine the Young's modulus of 2D materials, *Adv. Mater.* **31**, 1807150 (2019).
- [24] D. Akinwande, C. J. Brennan, J. S. Bunch, P. Egberts, J. R. Felts, H. Gao, R. Huang, J.-S. Kim, T. Li, Y. Li *et al.*, A review on mechanics and mechanical properties of 2D materials—Graphene and beyond, *Extreme Mech. Lett.* **13**, 42 (2017).
- [25] D. Çakır, F. M. Peeters, and C. Sevik, Mechanical and thermal properties of h-MX₂ (M = Cr, Mo, W; X = O, S, Se, Te) monolayers: A comparative study, *Appl. Phys. Lett.* **104**, 203110 (2014).
- [26] D. Li, Y. Zheng, H. Zhang, Z. Chen, and H. Ye, Commensurate stacking-induced ultrahigh yet discontinuous bending stiffness of the double-layer black phosphorus, *Appl. Surf. Sci.* **605**, 154729 (2022).
- [27] Z. Xu, Q.-S. Zheng, and G. Chen, Thermally driven large-amplitude fluctuations in carbon-nanotube-based devices: Molecular dynamics simulations, *Phys. Rev. B* **75**, 195445 (2007).
- [28] K. Cai, X. Li, J. Shi, and Q.-H. Qin, Nanospring from partly hydrogenated graphene ribbon: A molecular dynamics study, *Appl. Surf. Sci.* **541**, 148507 (2021).
- [29] J. Kang, S. Tongay, J. Zhou, J. Li, and J. Wu, Band offsets and heterostructures of two-dimensional semiconductors, *Appl. Phys. Lett.* **102**, 012111 (2013).
- [30] J. W. Jiang, Parametrization of Stillinger-Weber potential based on valence force field model: Application to single-layer MoS₂ and black phosphorus, *Nanotechnology* **26**, 315706 (2015).
- [31] J. W. Jiang, Z. N. Qi, and H. S. Park, Elastic bending modulus of single-layer molybdenum disulfide (MoS₂): Finite thickness effect, *Nanotechnology* **24**, 435705 (2013).
- [32] D. Li, H. Zhang, Y. Zheng, and H. Ye, Understanding the size and chirality dependence of bending stiffness of single-layer MoS₂ by a spring-driven method, *Phys. Rev. B* **106**, 144109 (2022).
- [33] T. Chang and H. Gao, Size-dependent elastic properties of a single-walled carbon nanotube via a molecular mechanics model, *J. Mech. Phys. Solids* **51**, 1059 (2003).
- [34] H. W. Zhang, J. B. Wang, and H. F. Ye, Influence of inversion energy on elastic properties of single-walled carbon nanotubes, *Mater. Sci. Eng., A* **467**, 78 (2007).
- [35] J. R. Xiao, B. A. Gama, and J. W. Gillespie, An analytical molecular structural mechanics model for the mechanical properties of carbon nanotubes, *Int. J. Solids Struct.* **42**, 3075 (2005).
- [36] H. Pan and Y.-W. Zhang, Edge-dependent structural, electronic and magnetic properties of MoS₂ nanoribbons, *J. Mater. Chem.* **22**, 7280 (2012).

- [37] V. Varshney, S. S. Patnaik, C. Muratore, A. K. Roy, A. A. Voevodin, and B. L. Farmer, MD simulations of molybdenum disulphide (MoS_2): Force-field parameterization and thermal transport behavior, *Comput. Mater. Sci.* **48**, 101 (2010).
- [38] S. Xiong and G. Cao, Molecular dynamics simulations of mechanical properties of monolayer MoS_2 , *Nanotechnology* **26**, 185705 (2015).
- [39] H. Bao, Y. Huang, F. Ma, Z. Yang, Y. Miao, K. Xu, and P. K. Chu, Size-dependent elastic modulus of single-layer MoS_2 nano-sheets, *J. Mater. Sci.* **51**, 6850 (2016).
- [40] M. Pelliciari, D. P. Pasca, A. Aloisio, and A. M. Tarantino, Size effect in single layer graphene sheets and transition from molecular mechanics to continuum theory, *Int. J. Mech. Sci.* **214**, 106895 (2022).
- [41] T. Li, Ideal strength and phonon instability in single-layer MoS_2 , *Phys. Rev. B* **85**, 235407 (2012).
- [42] Y. Li, P. Chen, H. Liu, J. Peng, F. Gao, and N. Luo, Wrinkling and failure behavior of single-layer MoS_2 sheets under in-plane shear, *Phys. Chem. Chem. Phys.* **21**, 19115 (2019).
- [43] H. Sun, P. Agrawal, and C. V. Singh, A first-principles study of the relationship between modulus and ideal strength of single-layer, transition metal dichalcogenides, *Mater. Adv.* **2**, 6631 (2021).
- [44] J.-W. Jiang and Y.-P. Zhou, Parameterization of Stillinger-Weber potential for two-dimensional atomic crystals, in *Handbook of Stillinger-Weber Potential Parameters for Two-Dimensional Atomic Crystals* (InTech, 2017), pp. 1–571.
- [45] S. B. Sharma, R. Paudel, R. Adhikari, G. C. Kaphle, and D. Paudyal, Structural deformation and mechanical response of CrS_2 , CrSe_2 and Janus CrSSe , *Physica E (Amsterdam, Neth.)* **146**, 115517 (2023).
- [46] J. Nian, L. Chen, Z. Guo, and W. Liu, Computational investigation of the lubrication behaviors of dioxides and disulfides of molybdenum and tungsten in vacuum, *Friction* **5**, 23 (2017).
- [47] B. Rahman Rano, I. M. Syed, and S. H. Naqib, Elastic, electronic, bonding, and optical properties of WTe_2 Weyl semimetal: A comparative investigation with MoTe_2 from first principles, *Results Phys.* **19**, 103639 (2020).
- [48] X. Li, M. Wu, B. Xu, R. Liu, and C. Ouyang, Compressive strain induced dynamical stability of monolayer 1T-MX_2 ($\text{M} = \text{Mo}, \text{W}$; $\text{X} = \text{S}, \text{Se}$), *Mater. Res. Express* **4**, 115018 (2017).
- [49] L. Yu, Q. Yan, and A. Ruzsinszky, Negative Poisson's ratio in 1T -type crystalline two-dimensional transition metal dichalcogenides, *Nat. Commun.* **8**, 15224 (2017).
- [50] J.-W. Jiang and H. S. Park, Negative Poisson's ratio in single-layer black phosphorus, *Nat. Commun.* **5**, 4727 (2014).